ACS APPLIED MATERIALS & INTERFACES

RESEARCH ARTICLE

www.acsami.org

Dissolution Kinetics of Polycrystalline Calcium Sulfate-Based Materials: Influence of Chemical Modification

Robin D. Fisher,[†] Michael M. Mbogoro,[†] Michael E. Snowden,[†] Maxim B. Joseph,[‡,§] James A. Covington,[‡] Patrick R. Unwin,[†,*] and Richard I. Walton[†,*]

[†]Department of Chemistry, [‡]School of Engineering, and [§]MOAC Doctoral Training Centre, University of Warwick, Coventry, CV4 7AL, United Kingdom

Supporting Information

ABSTRACT: Using a channel flow cell (CFC) system, the dissolution kinetics of polycrystalline gypsum-based materials have been examined with the aim of understanding their interaction with water, a property that limits the applications of the material in many situations. ICP (inductively coupled plasma) analysis of elemental concentrations in solution as a function of time yields surface fluxes by using a finite element modeling approach to simulate the hydrodynamic behavior within the CFC. After correction for surface roughness, a value for the intrinsic dissolution flux into water of pure polycrystalline gypsum, $CaSO_4.2H_2O$, of 1.1 ($\pm$0.4) $\times$ 10^{-8} mol cm^{-2} s^{-1} has been obtained. The addition of known humid creep inhibitors to the gypsum samples, including boric acid, tartaric acid and 3,4,5-trihydroxybenzoic acid (gallic acid), was found to have little measurable effect on the dissolution kinetics of gypsum: all yielded dissolution fluxes of 1.4 ($\pm$0.6) $\times$ 10^{-8} mol cm^{-2} s^{-1}. However, trisodium trimetaphosphate (STMP) was found to have a small detectable inhibitory effect relative to pure gypsum yielding a flux of 7.4 ($\pm$2.0) $\times$ 10^{-9} mol cm^{-2} s^{-1}. The data strongly suggest that models for humid creep inhibition that involve dissolution−crystallization of gypsum crystallites are less likely than those that involve a hindered ingress of water into the gypsum matrix. For comparison, composite materials that comprised of calcium sulfate anhydrite ($CaSO_4$) crystallites bound by a polyphosphate matrix were also studied. For some of these samples, Ca^{2+} surface fluxes were observed to be ~1 order of magnitude lower than values for polycrystalline gypsum control substrates, suggesting a useful way to impart water resistance to gypsum-based materials.

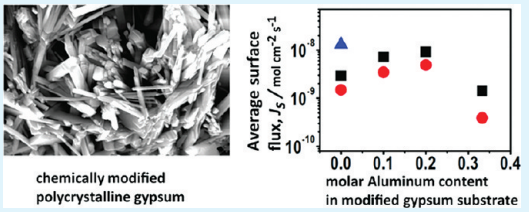

KEYWORDS: gypsum, humid creep, phosphate binder, composite, water resistance

INTRODUCTION

Gypsum, $CaSO_4 \cdot 2H_2O$, has been used since antiquity to line the interiors of buildings because of its many attractive properties such as ease of application, good thermal insulation, fire resistance, and its favorable processing conditions, requiring only moderate temperatures.[1] There is renewed interest in utilizing gypsum for exterior and load bearing applications given its availability as an industrial byproduct and the much lower processing temperatures compared to traditional silicate cements.[2] The property that restricts the wider use of gypsum is its poor water resistance. Gypsum objects are produced by the hydration of calcium sulfate hemihydrate to yield an interlocking mass of polycrystalline, needle-shaped gypsum particles.[3] A small amount of water, present as atmospheric humidity, is enough to cause a dramatic reduction in mechanical properties such as Young's modulus,[4] flexural strength,[5] compressive strength[6] and hardness.[5] Gypsum can also deflect or creep under an applied stress in the presence of water over long periods of time, a process that has been suggested to be responsible for the instability of old gypsum mines.[7] A similar phenomenon is also seen in industrial products where preformed shapes of polycrystalline gypsum, such as ceiling tiles, can deflect in high humidity environments, in a process known as "humid creep" or "sag", causing aesthetic as well as mechanical defect.[8]

A consensus on the exact mechanisms responsible for the humid creep of gypsum with moisture contact has not been reached. Badens et al. suggest that the bonds between crystals are weakened by the ingress of water at grain boundaries,[4] whereas Chappuis proposed a model involving local dissolution and recrystallization of gypsum in the surface water layers at the contact points between interlocking crystals.[9] Chemical additives, including tartaric acid,[10] boric acid,[11] sodium trimetaphosphate (STMP),[12] and 3,4,5-trihydroxybenzoic acid (gallic acid),[13] have been reported in the patent literature as means of inhibiting the macroscopic effect of humid creep. The mechanism of their mode of action is unclear, although in separate studies the presence of carboxylic acids, including tartaric acid, has been found to have an effect on the rate of crystal growth of gypsum.[4,14] From that work, it was proposed that carboxylate anions are able to bind to the surface of gypsum crystals, thus potentially modifying crystal habit as well as crystallization rate.[4,14] It is interesting to

Received: June 12, 2011
Accepted: August 23, 2011
Published: August 23, 2011

 © 2011 American Chemical Society

note that previous studies on other calcium minerals have shown that tartaric acid can also inhibit dissolution.[15]

In this paper, we study the dissolution of various modified gypsum materials to provide experimental values for the kinetics of dissolution. The effective dissolution rate is reliant on the interplay between surface reactivity of the substrate under investigation and mass transport conditions.[16,17] Reliable dissolution rates can be elucidated when the experimental techniques employed distinguish quantitatively between surface kinetic effects and mass transport.

The channel flow cell (CFC) system has been applied extensively in the study of dissolution processes.[15,18−29] Typically, this method involves positioning the substrate under investigation as the basal wall of a rectangular duct through which solution flows under laminar conditions. Dissolution rates and reaction kinetics are then elucidated by analyzing the flow rate dependent concentration of dissolved species (or reactant) downstream of the substrate. With a wide range of controllable mass transport rates, the dependence of dissolution rates on flow rate can be determined.[15,18−24] Furthermore, because of well-defined flow within a CFC chamber, it is possible to model the flow rate dependent convective-diffusion behavior and ultimately determine the validity of proposed rate laws that govern the dissolution reaction.[15,18−29] In the past, CFC designs have been susceptible to awkward assemblies (two-three part units with nuts, bolts or sealants needed) and restrictions on the size of samples which could be analyzed.[30] Here, we apply a recently developed CFC design that employs micro-stereolithography to fabricate miniaturized one-part CFC units.[31] This design avoids complicated assemblies and reduces the need for large cell volumes, without compromising mass transport conditions.

Herein, the CFC technique is combined with inductively coupled plasma-optical emission spectrometry (ICP-OES) for the determination of concentrations of dissolved Ca^{2+} (and PO_4^{3-} in some of the modified materials) originating from the substrate materials collected in the CFC effluent. Mass transport in the CFC is modeled by formulating convective-diffusion equations and defining a boundary condition for the dissolving substrate so as to predict the concentration of dissolved Ca^{2+} (and PO_4^{3-}) at a specific flow rate. By using this approach, a comparison can be made between experimental data and predictions from theory; ultimately offering mechanistic insights into the dissolution reaction and the ability to test the validity of rate equations. We have compared the effect of proprietary humid creep additives on gypsum, with an alternative approach to moisture inhibition which uses composite phosphate-bound calcium sulfate sub-hydrate crystallites. Aluminum phosphate has previously been used to bind SiC and AlN,[32] and glass fiber[33] to make high-temperature stable composites. Consequently, this represents an interesting prospect for improving the durability of gypsum-based materials. Our aim was to provide direct experimental data that might allow the various models proposed for the interaction between gypsum-based materials and water to be distinguished.

MATERIALS AND METHODS

Materials. *Materials Modified with Humid-Creep Additives.* DL-tartaric acid (Sigma-Aldrich), trisodium trimetaphosphate (STMP) (Sigma-Aldrich), 3,4,5-trihydroxybenzoic acid monohydrate (gallic acid, Sigma-Aldrich) and boric acid (Fisher Scientific) were dissolved in Milli-Q reagent grade water (Millipore) with a typical resistivity of ca.18.2 MΩ cm at 25 °C, to yield solutions of 1 mM. This concentration was chosen to compare the effectiveness of humid creep inhibitors in quantities similar to those reported in industrial applications.[10−13] Gypsum samples were cast by mixing α-plaster (94% calcium sulfate hemihydrate by TGA) with these humid creep solutions, such that water:plaster = 0.7:1 by weight. A control sample of similar ratio as the humid creep samples was also made where the plaster was mixed with pure water. Gypsum samples were produced by pouring the mixture into silicone molds (12 mm diameter and 24 mm height), which were left for 1.5 h to hydrate (conversion of $CaSO_4 \cdot 0.5H_2O$ into $CaSO_4 \cdot 2H_2O$). The cylindrical samples were then dried in an oven at 40 °C for 12 h, after which samples were impregnated under vacuum with low viscosity grade epoxy resin (Epofix) and allowed to cure. The compositions, by weight, of samples prepared in this way are summarized in Table 1.

Table 1. Composition of Humid Creep Additive Samples at a 1 mM Solution Concentration

sample	humid creep additive (%)	λ
gypsum control	0	1.5 ± 0.1
STMP	0.021	1.4 ± 0.3
tartaric acid	0.011	1.4 ± 0.2
boric acid	0.011	1.8 ± 0.2
gallic acid	0.013	1.3 ± 0.1

Table 2. Nominal Compositions of Composite Samples

mole fraction					
Ca	S	P	Al	Al: P	λ
0.40	0.40	0.21	0.00	0	1.8 ± 0.2
0.40	0.40	0.19	0.02	0.1	1.9 ± 0.2
0.40	0.40	0.17	0.03	0.2	1.6 ± 0.3
0.40	0.40	0.15	0.05	0.33	1.8 ± 0.5

Composite Phosphate Materials. Composite samples made with gypsum, aluminum dihydrogen phosphate and orthophosphoric acid (87% in water) in varying molar ratios were prepared by impregnating dry porous gypsum under vacuum; see Table 2. The samples were then dried at 40 °C for 12 h, after which they were crushed and pressed (10 MPa, 1 min) before heating up to 500 at 5 °C min^{-1} and holding there for 2hrs. All samples processed in this way were polished with silicon carbide 4000 grit paper (Buehler) as well as on a pad with 6 μm diamond spray (Kemet Int Ltd.), after which they were rinsed (1−2 s) in ultrapure H_2O. For each dissolution experiment, a fresh surface was fashioned by polishing the surface as described below.

Characterization. For all samples, powder X-ray diffraction (XRD) (D5000 Diffractometer, copper K-α radiation) analysis was carried out in order to identify characteristic Bragg peaks of known crystalline phases using the JCPDS Powder Diffraction File database V9, 2005. Fourier transform infrared (FTIR) (Perkin-Elmer Spectrum 100) analysis was performed on ground samples within the range of 4000−650 cm^{-1} (resolution 4 cm^{-1}), using a diamond ATR accessory. BET measurements were carried out on 1−2 g of roughly broken up sample in 12.7 mm diameter tubes. Porous gypsum samples were deaerated under a flow of N_2 gas at 45 °C for more than 12 h. Composite samples, on the other hand, were deaerated at 300 °C for 1 h.

Surface Roughness Normalization. For hydrodynamic dissolution studies, well-defined mass transport conditions are reliant on the sample under consideration not displaying significant roughness. It is also important to identify if the surface roughness changes over the course of the reaction as this could influence apparent dissolution kinetics.[34,35] In order to account for possible changes in surface roughness between

different substrates and over the course of dissolution reactions, surface area measurements were carried out via white light interferometry (WLI) (WYKO NT-2000 Surface Profiler, WYKO Systems), typically using a 10 × or 20 × objective. These measurements were carried out on the substrates both prior to, and immediately after, CFC experiments. The resulting topographical (3D) images of the sample surface were analyzed via a scanning probe image processor (SPIP Image Metrology, version 5.1.0). From these measurements, the surface roughness factor, λ (= real area/geometric area) could be determined and used to normalize dissolution data obtained from ICP analysis, by the exposed surface area of the dissolving substrate, thereby providing reliable dissolution rates.[16,17] Further information may be found in the Supporting Information, section 2.

Microscopy. Samples were visualized via scanning electron microscopy (SEM) (EVO 50 XVP Zeiss Supra 55-VP) at 20 keV. Prior to SEM analysis, each sample was coated with a thin layer of carbon and a copper strip was attached to provide a conductive path to ground. Quantitative analysis of surface composition was carried out using energy dispersive X-ray analysis (EDXA) (Inca X-sight, Oxford Instruments). In the case of samples modified with humid creep additives, EDXA was carried out to determine the relative amount of resin and gypsum crystal on the surface using the backscattered electron detector, and then binarizing with ImageJ image processing software. For the composite samples, EDXA allowed an estimation of the elemental composition of the surface in order to track any changes after dissolution.

Dissolution Procedure. Dissolution experiments were carried out using a CFC, whose design and fabrication has recently been described elsewhere.[31,36] Figure 1a shows in cross-section the CFC, highlighting the sample position and an in-built mixer in the outlet which ensured solution exiting the CFC was homogeneous, whereas (b) is schematic of the finished CFC unit that is placed on top of the sample to assemble the cell. The geometric sample area exposed to flowing solution was determined by the internal dimensions of the channel for which the length (l) and width (w) were 10 mm and 4 mm, respectively. The channel height ($2h$), determined via WLI, was 210 μm.

To assemble the setup, the CFC was placed on the sample of interest and held in place by a clamp. Tubing (PVC, Saint-Gobain Plastics) connecting to the CFC inlet and outlet were simply push fitted and attached to a syringe pump to deliver solutions at well-defined rates via Omni-fit adapters (Bio-Chem Fluidics). The syringe pump (KD Scientific) was equipped with a 50 mL syringe (BD Plastipak, luer-Lok) with a 22 mm inner diameter. For all experiments, flow rates (V_f) were varied from 0.008 to 0.0167 $cm^3\ s^{-1}$, which amounted to a maximum contact time of ~1 s between the exposed crystal surface and the flowing solution in the channel (mean flow rate). This short contact time allowed for numerous measurements to be made over a wide range of flow rates. Solution at the outlet was collected in aliquots (~ 5 mL) at set intervals, for all flow rates, and trace element analyses of dissolved Ca^{2+} and phosphorus) were carried out on the aliquots via ICP-OES (Perkin-Elmer Optima 5300 DV). This allowed for extraction of flow-rate dependent output concentrations, from which dissolution fluxes were determined. For ICP-OES analysis, standards used for Ca and P were prepared from 1 g dm^{-3} stock solutions supplied by Fluka.

THEORY AND KINETIC MODELING

All computer simulations were designed and executed on a Dell Intel core 2 Quad 2.49 GHz computer equipped with 8GB of RAM and running Windows XP Professional X64 bit 2003 edition. The commercial finite element modeling package Comsol Multiphysics 3.5a (Comsol AB, Sweden) was used to perform simulations, using the Matlab interface (Release 2009b) (MathWorks Inc., Cambridge, UK). Simulations were executed with >51 000 triangular mesh elements where the resolution of

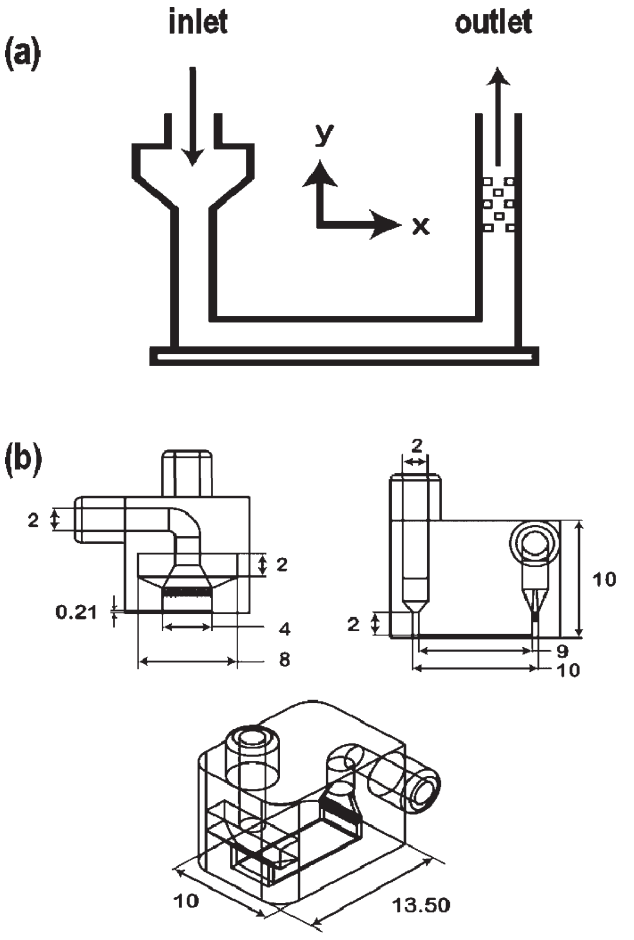

Figure 1. (a) Illustration of the two-dimensional domain with the cross section of the flow cell (not to scale) highlighting a small reservoir at the inlet and mixer at the outlet, as well as the crystal substrate along the base of the channel. (b) Schematic of the CFC design from several viewpoints, where the cell dimensions are in mm.

the mesh was defined to be finest in the vicinity of the basal plane of the channel, effectively along the surface of the crystal substrate.

Due to the CFC geometry, the channel was simulated as a 2D cross-section along the channel length as illustrated in Figure 1(a). A 3D model was unnecessary since the channel dimensions were $w \gg h$, such that edge effects in the $w(x)$ direction were assumed to be negligible. The hydrodynamic behavior within the channel is described in detail elsewhere.[31] Briefly, incompressible Navier–Stokes equations for momentum balance and continuity were solved under steady-state conditions, to yield solution velocities within the channel. The resultant velocity profile was used in the convection–diffusion equation to predict mass transport within the CFC.

The convective-diffusion equation was solved for the simulated domain (Figure 2a) under steady-state conditions

$$D_i \nabla^2 C_i - \mathbf{V} \cdot \nabla C_i = 0 \qquad (1)$$

where D_i is the diffusion coefficient of the species of interest, i, and C_i is its concentration. The dissolving species quantified by ICP analysis were Ca^{2+} (for all materials) and phosphate (for the phosphate-modified materials). A diffusion coefficient of $0.792 \times 10^{-5}\ cm^2\ s^{-1}$ was used for Ca^{2+} and $0.759 \times 10^{-5}\ cm^2\ s^{-1}$ for HPO_4^{2-} which was considered the dominant phosphate ion.[37]

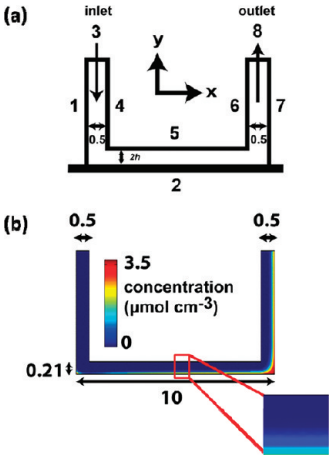

Figure 2. Two-dimensional representation of (a) the channel geometry used for finite element simulations, where the numbers represent the domains as described in text, and (b) concentration profile along the channel at $V_f = 0.008$ cm^3 s^{-1} and $k = 7 \times 10^{-9}$ mol cm^{-2} s^{-1}. The cell dimensions are in millimeter.

Table 3. Boundary Conditions Describing Convective-Diffusion in the Flow Cell[a]

	convective-diffusion boundary conditions	
boundary	condition	governing equation
1	insulation	$nN = 0$
2	diffusive flux	$nN = k$
3	inlet	$C_i = C_b$
4	insulation	$nN = 0$
5	insulation	$nN = 0$
6	insulation	$nN = 0$
7	insulation	$nN = 0$
8	outlet	$n(-D_i \nabla C_i) = 0$

[a] n is the vector normal to the boundary, N is the flux, k (mol cm^{-2} s^{-1}) is a heterogeneous rate constant, and C_b is the bulk concentration. The numbers refer to the labels in the simulated domain (Figure 2) and used in the text.

V is the velocity vector with components u and v in the x and y direction, respectively, and ∇ is the vector differential operator. The boundary conditions used to describe the convection-diffusion problem in the CFC are summarized in Table 3. Boundaries 1 and 4−7, as illustrated in Figure 2a, represent inert walls of the channel. Boundary 3 is the channel inlet where fresh solution enters the channel, boundary 2 is the exposed crystal surface where dissolution occurs and boundary 8 is the channel outlet; mass transport across this boundary is due to convection only. Note that the condition on boundary 2 introduces a simple dissolution flux (rate constant, k). This contrasts with our recent work on single crystal gypsum where we considered a rate law that was first-order in interfacial undersaturation.[38] The approach herein is reasonable because first, we study the dissolution reaction far from equilibrium (approaching zero saturation levels across the entire crystal surface) at the crystal/solution interface in the case of gypsum and second, for the composite materials, we do not know the solubility explicitly, so a straightforward flux approach is optimal. We were able to confirm the veracity of this simple model by virtue of the fact that measurements are made over a wide range of mass transport rates in the CFC method, and by the fact that intrinsic fluxes deduced are consistent with earlier work (where comparisons can be made)[16,17] and our own recent CFC studies.[38]

RESULTS AND DISCUSSION

Materials Characterization. *Gypsum with Humid-Creep Additives.* Characterization of samples with powder XRD was carried out to verify the nature of the crystalline phase(s) present. Because of sample preparation, processing procedures and known effects of some humid creep additives on the hydration of plaster, it was possible that various calcium sulfate materials, such as the hemihydrate ($CaSO_4.0.5H_2O$) or anhydrite ($CaSO_4$), may have formed by dehydration (loss of crystal lattice H_2O) or incomplete hydration.[39] Powder XRD showed that gypsum was the only crystalline phase present in all samples. There was no trace of any calcium carboxylate phase present in the samples prepared with tartaric or 3,4,5-trihydroxybenzoic acid (gallic acid), which is not surprising given the low level of additive used (see Table 1). FTIR analysis similarly was unable to detect any effect of the humid creep additives. XRD and FTIR results can be found in the Supporting Information, section 1. Sample preparation, as described above, involved the impregnation of samples with Epoxy resin: the aim was to minimize the effect of porosity and potential ingress of solution into the bulk sample so as to limit dissolution studies to the intrinsic surface kinetics of the polycrystalline materials. Polycrystalline cast gypsum objects are known to be highly porous (typically 36−61% by Hg porosimetry) at the water: plaster mixing ratios typically used to retain fluidity.[40] The surface composition of gypsum relative to resin was approximately 1:1 for all samples apart from those treated with tartaric acid where the ratio was 1:1.5. Further details are given in the Supporting Information, section 2, which also details λ values for each of the materials studied (see also Table 1).

It is important to note that the length scale of the heterogeneity in the surface presented to solution is relatively small and comparable to the size of the concentration boundary layer over much of the surface, for all of the flow rates (Figure 2b), so that the surface can be treated as uniformly active for the purposes of the dissolution model.

Composite Materials. The composite materials produced in this study were made up in varying ratios of Al and phosphate, to gypsum. Figure 3 shows (a) XRD patterns and (b) FTIR spectra for all samples. Powder XRD (Figure 3a) shows the crystalline component of these samples is not gypsum but rather calcium sulfate anhydrite, $CaSO_4$, and in the case of the highest aluminum content (Al:P = 0.33), hemihydrate, $CaSO_4 \cdot 0.5H_2O$, is also present. This suggests that significant Al quantities (Al:P > 0.2) prevents the complete dehydration of gypsum to anhydrite up to 500 °C, possibly through a reduction of the thermal conductivity which would lower the temperature of the center of the pellet. Dehydration of calcium sulfate hydrates is known to occur at lower temperatures in acidic conditions,[41] consistent with our observations: the solutions containing the least Al were the most acidic and may have caused the dehydration to anhydrite before the binder and coating had cured. No crystalline phosphates were detected in these samples by XRD. From FTIR analysis, Figure 3b, two bands characteristic of SO_4^{2-} present in anhydrite at approximately 1100 and 670 cm^{-1}, were assigned for all samples.[42] The existence of hemihydrate in the Al:P = 0.33 sample was confirmed

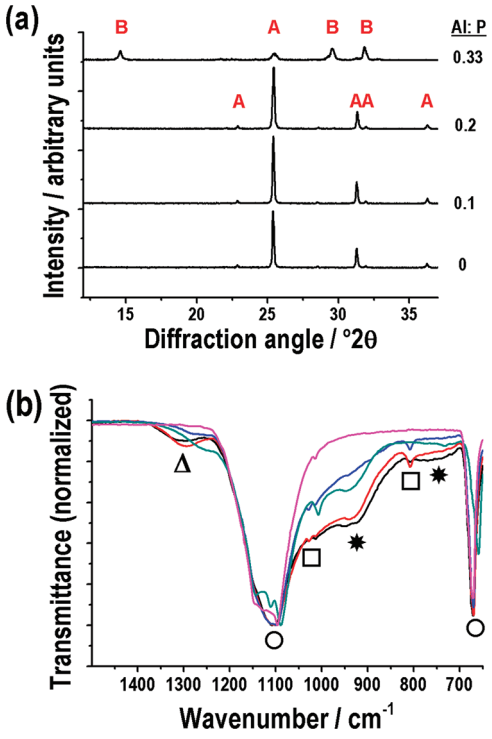

Figure 3. Analysis of the composite samples by (a) XRD, showing the crystalline phases, where A = anhydrite and B = bassanite ($CaSO_4 \cdot 0.5H_2O$), and (b) FTIR spectra of phosphate composite materials with ratios of Al: P = 0 (black), 0.1 (red), 0.2 (blue), 0.33 (green), and anhydrite reference (purple), where the symbols ○, □, △, and * represent SO_4^{2-}, $Al(PO_3)_3$, P═O, and P−O−P, respectively.

from a shifted SO_4^{2-} band at 660 cm^{-1}, and the crystal water at 3610, 3555, and 1619 cm^{-1}.[42]

The most useful information obtained from FTIR concerned the phosphate binder, which was found to comprise of polyphosphate. For bands assigned to P−O−P (∼945 and ∼760 cm^{-1}) and P═O (∼1300 cm^{-1}) bonds,[43,44] there tended to be a lower relative intensity with increasing Al content, expected because metals such as Al are known to break up this P−O−P network in phosphate glasses, forming more stable P−O−Al linkages instead.[45,46] The Al:P = 0.1 and 0.2 samples, however, were not completely amorphous: there was evidence for a crystalline phase from the small peaks appearing at 1028 and 808 cm^{-1}. The same bands have been observed by Han et al. when heating $Al(H_2PO_4)_3$ to 250−300 °C, and were assigned, respectively, to asymmetric and symmetric stretching of P−O−P within a metaphosphate $Al(PO_3)_3$ ring structure.[43] The small peak at 1007 cm^{-1} in the Al:P = 0.33 sample appears to be a shifted asymmetric stretching of the linear P−O−P chain, also observed by Han et al.[43] $Al(PO_3)_3$ polymorphs have been observed by XRD and ^{31}P MAS NMR after heating similar mixtures in excess of acid,[47,48] consistent with our findings. No Bragg peaks characteristic of $Al(PO_3)_3$ were observed in Figure 3a, so the quantity or average crystallite size must have been too low for detection by XRD.

Sample composition was found to have dramatic effects on the microstructure as observed via SEM. Figure 4 shows SEM images of composite materials with Al: P ratios of: (a) 0, (b) 0.1, (c) 0.2, and (d) 0.33. Samples exhibited a denser and more homogeneous microstructure at low Al content (Figure 4a), becoming increasingly less compact and heterogeneous as the amount of Al increased (Figure 4b−d). During sample processing, it was noticed that at lower Al content, samples were easier to grind and press. This may be attributed to the rapid readsorption of H_2O from the atmosphere due to the hygroscopic nature of the dried phosphoric acid. Figure 5 plots the change in porosity and BET surface area as a function of Al content. Both porosity and surface area were found to increase with increasing aluminum content, corroborating SEM observations.

Figure 6 shows the EDXA elemental analysis of composite materials with Al: P ratios of: (a) 0, (b) 0.1, (c) 0.2, and (d) 0.33, for regions on the sample surface directly exposed to etching solution during CFC measurements, as well as inactive areas (far away from where the CFC unit was positioned on the sample surface). For most samples (Figure 6a−c) dissolved regions (0−3 mm on *x*-axis) exhibited no change in the relative ratio of elements (Al, P, S and Ca) compared to inactive regions which predictably correlated with expected values (Table 2). This observation suggests that there was no preferential dissolution of any particular element over others in the sample. However, at the highest Al: P ratio (0.33), it appeared that the calcium sulfate scaffolding dissolved preferentially relative to the phosphate binder (Figure 6(d). This point is discussed later.[16,49]

Dissolution Kinetics. *Insights from Simulations.* We have fully described mass transport in the CFC utilized: after a short lead-in length, a steady laminar Poiseulle velocity is established and maintained along the channel.[38] Figure 2b shows a typical concentration profile of dissolved Ca^{2+} at a flow rate of 0.008 $cm^3\ s^{-1}$, and $k = 7 \times 10^{-9}$ mol $cm^{-2}\ s^{-1}$. The concentration distribution near the reactive substrate becomes more diffuse with increasing distance downstream. Over much of the substrate, the concentration boundary thickness is less than or of the order of the surface heterogeneity of the samples, confirming the validity of the model utilized which treats the surface as uniformly active (with subsequent correction for the exposed active substrate surface area); see the Supporting Information, section 3, for further information and analysis.

Figure 7 is a 3D plot of the outlet concentration as a function of applied rate constant k (mol $cm^{-2}\ s^{-1}$) and volume flow rate, V_f ($cm^3\ s^{-1}$) predicted from simulations. It is evident that an increase in k results in an increase of outlet concentrations for any flow rate. This is a consequence of the increase in the rate of generation of dissolution products from the crystal surface. Furthermore, the highest outlet concentrations are seen for the lowest V_f (0.008 $cm^3\ s^{-1}$) values, because of the longer interaction between the crystal surface and etching solution, resulting in an accumulation of dissolved species.

Surface Area Analysis. WLI measurements were carried out in order to determine the surface roughness factor, λ of all substrates. This technique is powerful, with a lateral resolution of 0.5−1.2 μm (at 10 × magnification) and a vertical resolution of ∼5 nm. Significant changes to surface roughness could influence the hydrodynamic character along the CFC channel, as well as affect the value of the reactive surface area exposed to solution during dissolution. To this end, λ was determined both prior to and after CFC experiments, to establish the extent of any surface roughening due to dissolution. Prior to dissolution, it was found that, λ ranged from 1.1 to 1.8 and 1.2 to 1.8 for the humid creep and composite surfaces, respectively. After dissolution measurements, λ remained largely within the pre-etching range at values of 1.2−2.1 and 1.5−2.8 for the humid creep and phosphate binder surfaces, respectively. For the purposes of normalizing

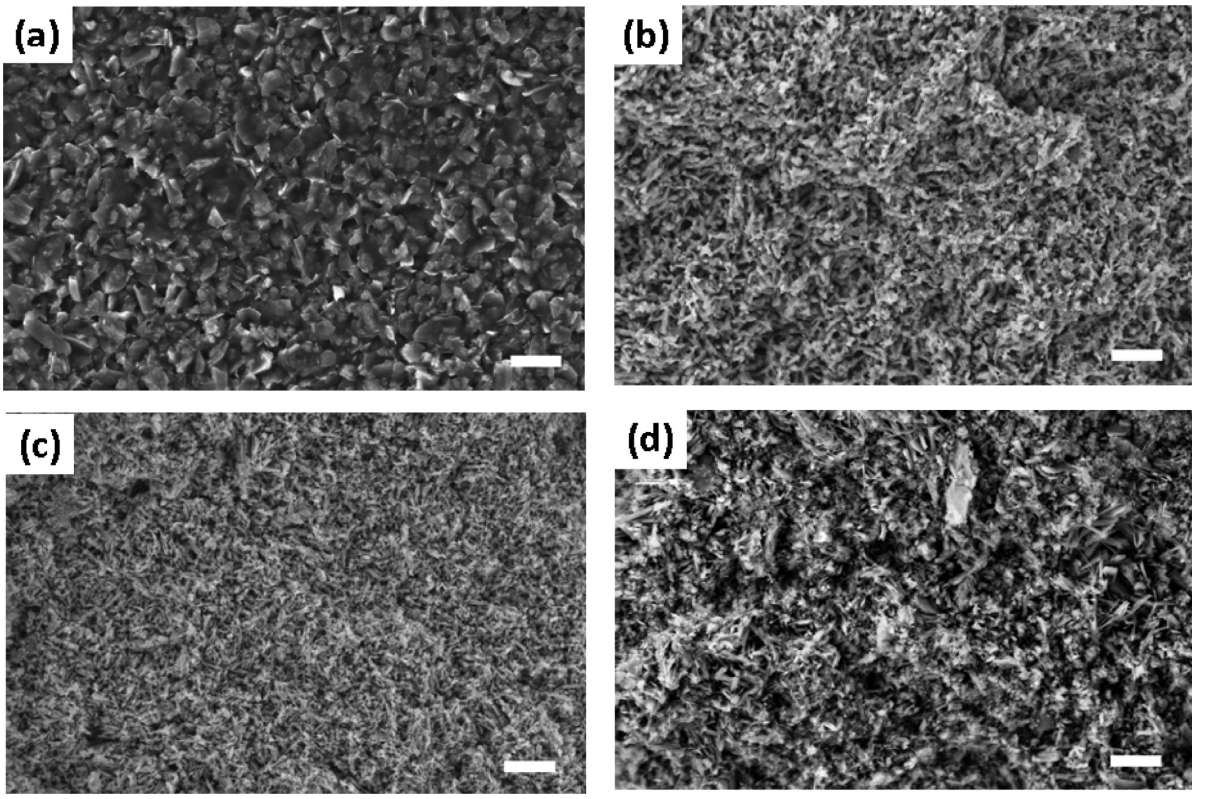

Figure 4. SEM images of a fractured pellet surface for the compositions Al: P = (a) 0, (b) 0.1, (c) 0.2, and (d) 0.33. The scale bar represents 20 μm.

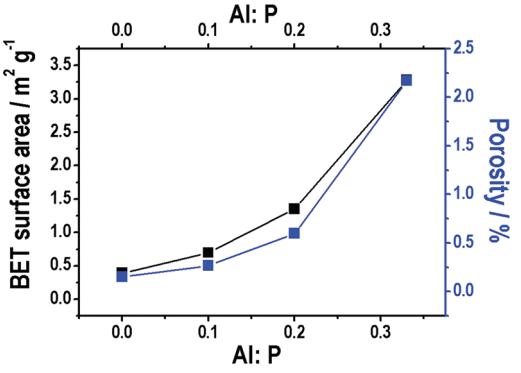

Figure 5. BET surface area (black) and porosity (blue) as a function of Al content in phosphate binder materials.

dissolution data, the mean λ value obtained from the two measurements (before and after dissolution) was used (see the Supporting Information, section 2).

The impact of surface recession on CFC hydrodynamics was determined by estimating the relative change in the channel height due to dissolution. The roughest surface (highest $\lambda = 2.8$) yielded an rms roughness value of 4.6 μm, which equates to ~2% of the channel height (210 μm). A study by Bruckenstein on rotating disk (RD) electrodes found that up to $\lambda = 7.5$, the reaction was not adversely affected by the surface roughness[50] and because the CFC and RD[51] exhibit similar mass transport rates, the sample roughness would not be an issue.

Although the intrinsic surface dissolution fluxes (J_s, mol cm^{-2} s^{-1}) can be obtained by normalizing the theoretical rate constants (k, mol cm^{-2} s^{-1}) values obtained from computer simulations by dividing by λ, this treatment of data was adequate for the composite sample set. Due to the presence of the inert resin matrix in the case of samples impregnated with humid creep additives, the flux measured was further normalized to account for the fraction of the surface which was active, i.e., $J_s = k/(\lambda\varphi)$, where φ is the fraction of exposed surface area (crystalline gypsum) across the sample. Further details are described in the Supporting Information, section 2.

Gypsum Modified by Humid-Creep Inhibitors. The effluent from CFC experiments was analyzed via ICP-OES to obtain for flow rate-specific concentrations of Ca^{2+}. For each sample, at least four replicate runs were made. Figure 8a) shows typical plots of average outlet concentrations as a function of flow rate; and the solid line corresponds to the best fit of applied k (mol cm^{-2} s^{-1}) obtained from the complementary simulations described above. The error bars are the result of two standard deviations calculated from at least four data sets. Once the theoretical rate constant, k, had been determined, average surface fluxes, J_s (mol cm^{-2} s^{-1}) were deduced by normalizing predicted data with respect to the exposed surface area and the surface roughness factor (λ), vide supra.

The values of J_s for all chemically modified samples are summarized in Figure 8(b), in which polycrystalline gypsum was observed to exhibit $J_s = 1.1\ (\pm 0.4) \times 10^{-8}$ mol cm^{-2} s^{-1}. Colombani recently reviewed various gypsum dissolution studies with the goal of reconciling discrepancies between them in the rates derived, along with newly measured values using holographic interferometry, and showed that when properly normalized for surface area effects (λ), all studies gave a consistent value of $J_s = 7 \times 10^{-9}$ mol cm^{-2} s^{-1} compared to $J_s = 5\ (\pm 2) \times 10^{-9}$ mol cm^{-2} s^{-1} obtained from new measurements.[16] The values

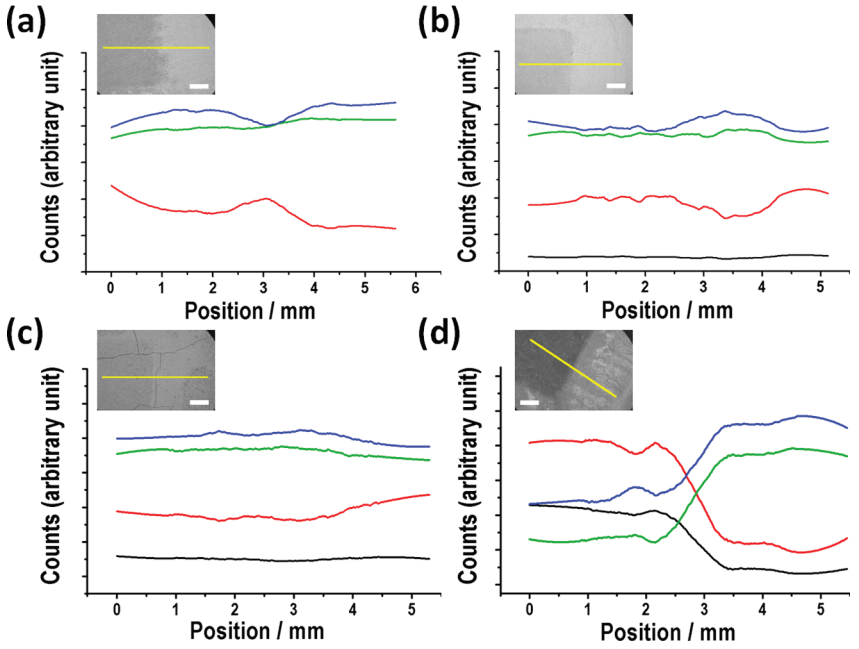

Figure 6. EDXA linescan results from composite materials with ratios of Al: P at (a) 0, (b) 0.1, (c) 0.2, and (d) 0.33, with the position of the linescan shown (inset) and the line colors refer to calcium (green), phosphorus (red), sulfur (blue), and aluminum (black). The scale bar represents 1 mm. Scanning was from left (within the CFC) to right (out of the CFC).

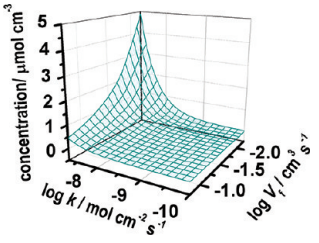

Figure 7. Simulated outlet concentrations as a function of applied rate constant, *k*, and flow rate as predicted from finite element simulations, which are based on the parameters in Figure 2a.

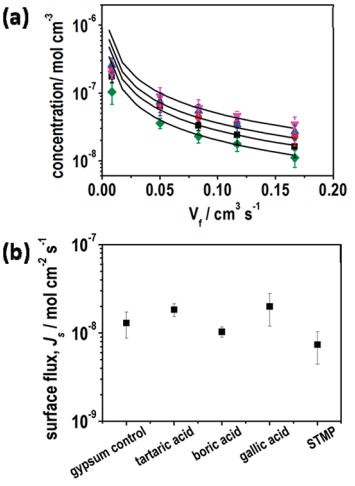

Figure 8. Plots of (a) Ca^{2+} outlet concentration as a function of flow rate for the dissolution of polycrystalline gypsum impregnated with humid creep inhibitors. The solid lines correspond to best fits to the model with rate constants in *k* (mol cm^{-2} s^{-1}) in the range of 8.6 (± 3.6) × 10^{-9} mol cm^{-2} s^{-1} for all humid creep samples, and the samples were gypsum control (black), STMP (green), tartaric acid (red), boric acid (blue), 3,4,5-trihydroxybenzoic acid (gallic acid) (pink), and STMP (green). These values were normalized with respect to surface area (λ), to yield (b) the average surface fluxes J_s of 1.3 (±0.4) × 10^{-8} mol cm^{-2} s^{-1} for the gypsum control, and 1.8 (±0.3) × 10^{-8} mol cm^{-2} s^{-1}, 1.0 (±0.1) × 10^{-8} mol cm^{-2} s^{-1} and 2.0 (±0.6) × 10^{-8} mol cm^{-2} s^{-1} and 7.4 (±0.4) × 10^{-9} mol cm^{-2} s^{-1}for the humid creep samples impregnated with tartaric acid, boric acid, 3,4,5-trihydroxybenzoic acid (gallic acid), and STMP, respectively.

obtained in the current work are in reasonable agreement with those previously reported, giving confidence in the surface area normalization and allowing meaningful comparisons to be made with the modified samples. That the values are slightly higher can be attributed to the polycrystalline nature of the substrates used, as well as the exposure of highly reactive planes on dissolving crystallites.

For gypsum materials modified with humid creep modifiers, J_s was found to be relatively similar, in the range 1.4 (±0.6) × 10^{-8} mol cm^{-2} s^{-1} with STMP exhibiting a small retarding effect on gypsum dissolution compared to the other inhibitors, yielding J_s = 7.4 (±2.0) × 10^{-9} mol cm^{-2} s^{-1}. The influence of STMP on gypsum dissolution kinetics corroborates our recent work, where STMP in solution was found to retard the dissolution kinetics of the (010) basal plane of gypsum, particularly in the [010], [001], and [100] directions.[38] The inhibitory effect measured here is somewhat less because there is no inhibitor in the solution; rather there is a finite (small amount) in the material that will be released during dissolution. The lack of a discernible retardation of dissolution due to the presence of humid creep additives (except from the small effect of STMP noted), casts some doubt on the dissolution−precipitation theory proposed by Chappuis to explain the mode of action of humid creep inhibition in

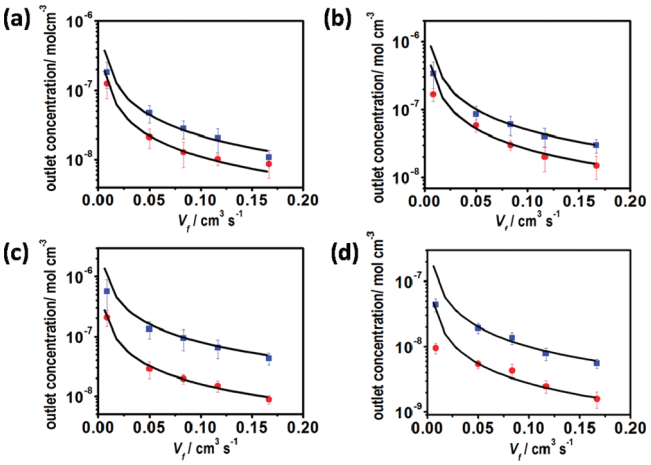

Figure 9. Plots of outlet concentrations of calcium (blue) and phosphorus (red) as a function of flow rate for the phosphate binder samples where the Al: P ratio was (a) 0, (b) 0.1, (c) 0.2, and (d) 0.33. The solid lines correspond to the best fit to the model with fixed flux k (mol cm^{-2} s^{-1}). Values for k are shown in Table 4.

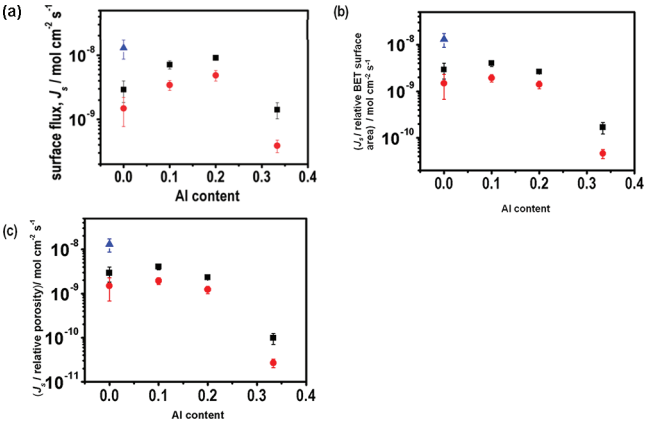

Figure 10. Plots of (a) dissolution fluxes, (b) dissolution fluxes normalized with respect to relative BET surface area, and (c) dissolution fluxes normalized with respect to relative sample porosity. The rates of Ca^{2+} (black) and PO_4^{3-} (red) as a function of Al content for all binder composites are shown. The calcium fluxes from polycrystalline gypsum control (blue) are also shown. The relative porosity and BET surface areas are defined with respect to the values for the gypsum control.

industrial gypsum products.[9] Another proposal is that the additives alter crystal habit and therefore the faces in contact with each another;[39] however, no additive produced a significant crystal habit modifying effect from our SEM results (see the Supporting Information, S2). The net effect of crystal habit modification may be to increase the total adhesion between crystals according to Finot et al. who determined that the adhesion between crystal faces was dependent on the combination in contact.[52] Indeed, Kato et al. found that other polar liquids such as ethanol also reduced the mechanical properties, to an extent in correlation with the liquid polarity.[53] Reynauld et al. used internal friction measurements to later postulate a visco-elastoplastic rheological model to describe the plastic flow of gypsum, where the absorbed liquid layer shields the electrostatic interactions between crystals and they slide past one another under stress.[54]

Badens et al. proposed that tartaric acid adsorbs on the (120) and (111) faces of gypsum, based on the most stable conformations of the molecule and the interatomic distances of calcium ions in the gypsum lattice.[14] Through molecular modeling, it has been predicted that the surface energy of most faces of gypsum (apart from the most stable (010) plane)[54] decreases when calcium tartrate is formed.[55] It follows from our results, and this discussion, that the mode of action of humid creep inhibition may be to reduce the amount of water present in the intercrystal region, thereby preventing loss of mechanical strength. Indeed Badens et al. also proposed that the humid creep inhibitors reduce the thickness of the absorbed water film on the crystallite surface,[4] which could be by the displacement of water molecules, as proposed by van der Voort and Hartman for gypsum crystallizing in the presence of organic impurities.[56] On the basis of our dissolution studies, this appears to be the most plausible explanation for the mode of action of humid creep inhibitor additives.

Composite Materials. Figure 9 shows typical plots of the average outlet concentration values for calcium and phosphate as a function of flow rate for the gypsum-composite materials, where the Al: P ratio was (a) 0, (b) 0.1, (c) 0.2, and (d) 0.33, and the solid lines correspond to the best fit k (mol cm^{-2} s^{-1}) as predicted from simulations, with the values shown in Table 3. For all samples, it was found that outlet concentrations of calcium were higher than those of phosphate, due to the sample composition (Ca:P ratio) as seen in Figure 6 and Table 2. However, the outlet concentration values in sample Al:P = 0.33 showed an apparently larger difference between calcium and phosphate, further corroborating observations made from Figure 6d, where the surface composition of calcium had decreased dramatically in the area exposed to solution.

Surface-area normalized fluxes, J_s, for the dissolution of calcium and phosphate ions from the composite materials are shown in Figure 10a, along with the corresponding value obtained for the polycrystalline gypsum control sample, for comparison. In this case, it is also possible to take account of possible influences of BET surface area or porosity on the measured fluxes, normalizing J_s values with respect to the intrinsic values for each of the materials, as has been done in Figure 10b,c. This has two effects compared to the J_s values alone: first it appears that the highest Al content has an apparently bigger influence in retarding dissolution, whereas the other compositions have more similar dissolution rates (within experimental error). All of these data highlight the difference between the release rates of PO_4^{3-} and Ca^{2+} from the phosphate bound materials upon dissolution, and clearly show how the dissolution of these composites vary significantly depending on the Al:P ratio used, as well as the morphology of the samples. At Al:P = 0, surface fluxes were found to be $J_s = 2.9\ (\pm 1.1) \times 10^{-9}$ mol cm^{-2} s^{-1} and $J_s = 1.5\ (\pm 0.7) \times 10^{-9}$ mol cm^{-2} s^{-1} for Ca^{2+} and PO_4^{3-}, respectively, which were ~1 order of magnitude lower than polycrystalline gypsum control ($J_s = 1.1\ (\pm 0.4) \times 10^{-8}$ mol cm^{-2} s^{-1}). The anhydrite crystallites in this composite matrix can be envisaged as being protected by a phosphate coating which, based on FTIR and XRD results (vide supra), was amorphous in nature. As the Al: P content increased to 0.1 and 0.2, Ca^{2+} dissolution rates approached values similar to the gypsum control (Figure 10a) with $J_s = 7.1\ (\pm 1.1) \times 10^{-9}$ mol cm^{-2} s^{-1} and $J_s = 9.1\ (\pm 0.6) \times 10^{-9}$ mol cm^{-2} s^{-1} for the Al:P = 0.1 and 0.2 substrates, respectively. These higher rates may have resulted due to the crystalline $Al(PO_3)_3$ (as determined via FTIR, vide supra) creating heterogeneity within the coating and, therefore less protective of the calcium sulfate from contact with impinging water in the

Table 4. Theoretical Flux Predictions from Simulations for Composite Binder Materials

sample		theoretical flux k (mol cm^{-2} s^{-1})	
Al: P	Ca: P	Ca^{2+}	PO_4^{3-}
0	1.9	$5.4 (\pm 2.0) \times 10^{-9}$	$2.8 (\pm 1.5) \times 10^{-9}$
0.1	2.1	$1.3 (\pm 0.2) \times 10^{-8}$	$6.5 (\pm 0.9) \times 10^{-9}$
0.2	2.4	$1.5 (\pm 0.7) \times 10^{-8}$	$8.0 (\pm 1.5) \times 10^{-9}$
0.33	2.67	$2.5 (\pm 0.7) \times 10^{-9}$	$6.9 (\pm 1.5) \times 10^{-10}$

channel. Indeed, when the porosity or BET-normalized surface fluxes are compared, there is little difference between Al:P = 0.0, 0.1, and 0.2. In contrast, the most striking result is the Al:P = 0.33, which has the stoichiometric quantity of elements for $Al(H_2PO_4)_3$, and is substantially amorphous and chemically stable[48] and seemed to provide the most protection of the coating for the anhydrite crystallites. This conclusion is further supported by the lower surface fluxes obtained at this Al:P ratio compared to corresponding values at lower Al content and, furthermore, by the pronounced discrepancy in Ca^{2+} and PO_4^{3-} surface fluxes with J_s = $1.4 (\pm 0.4) \times 10^{-9}$ mol cm^{-2} s^{-1}and $J_s = 3.9 (\pm 0.8) \times 10^{-10}$ mol cm^{-2} s^{-1} for Ca^{2+} and PO_4^{3-} ions, respectively (see Table 4). It was pointed out earlier (Figure 6d) that the calcium mineral dissolved preferentially to the phosphate binder and this means that surface composition changes throughout the dissolution measurements. Nonetheless, a reasonable fit and analysis of the kinetics appears to be possible. The release rates for calcium and phosphate were a factor of 2−3 slower than in the case where Al: P = 0 and, moreover, ∼ 1 order of magnitude lower than the gypsum reference sample. This effect is even more striking when one considers that the Al:P = 0.33 material exhibits much higher BET surface area and porosity than the other materials (Figure 5).

CONCLUSIONS

We have shown how a novel channel flow cell technique can be applied to study the dissolution behavior of industrially relevant materials. We find that the simple flux rate law applied herein describes adequately the dissolution kinetics of unmodified polycrystalline gypsum and yields intrinsic dissolution flux values that compare well to values obtained in literature. Modification of polycrystalline gypsum with a variety of established humid creep inhibitors has a minimal influence on dissolution kinetics under the experimental conditions applied, suggesting that a simple dissolution−precipitation model of moisture interaction with gypsum does not explain the mode of action of humid creep inhibitors. Models involving the surface binding of additives that reduce water adsorption in the intercrystal region are more reasonable.

Novel gypsum-based composites with phosphates have been produced, characterized and tested using the CFC method. Compared to polycrystalline gypsum and anhydrite controls, these show lower dissolution fluxes, which is an essential requirement for the development of robust materials for the future, and thus constitute a promising avenue for further exploration in this respect.

ASSOCIATED CONTENT

Supporting Information. Further analysis of chemically modified gypsum substrates, along with a quantitative assessment of the substrate surface heterogeneity. This material is available free of charge via the Internet at http://pubs.acs.org/.

AUTHOR INFORMATION

Corresponding Author

*E-mail: p.r.unwin@warwick.ac.uk (P.R.U.); r.i.walton@warwick.ac.uk (R.I.W.).

Author Contributions

The authors Robin D. Fisher and Michael M. Mbogoro contributed equally to this work.

ACKNOWLEDGMENT

This work was funded by Saint-Gobain Gyproc and the EPSRC Collaborative Training Account at the University of Warwick. M.J. was supported by the EPSRC-funded MOAC Doctoral Training Centre. We thank L. Song and P. Aston for assistance with ICP-OES, and K. McKelvey for help and advice on image analysis in the Supporting Information. We also thank H. Jaffel and J.-B. Denis at St. Gobain for helpful discussions. The WLI and ICP-OES equipment used in this research was obtained through Birmingham Science City with support from Advantage West Midlands and the European Regional Development Fund.

REFERENCES

(1) Arpe, H.-J. In *Ullmans Encyclopaedia of Industrial Chemistry*, 5th ed.; VCH: Weinheim, Germany, 1985; Vol. A4, p 555.
(2) Escalante-Garcia, J. I.; Magallanes-Rivera, R. X.; Gorokhovsky, A. *Constr. Build. Mater.* **2009**, *23*, 2851.
(3) Gartner, E. M. *Cem. Concr. Res.* **2009**, *39*, 289.
(4) Badens, E.; Veesler, S.; Boistelle, R.; Chatain, D. *Colloid Surf., A* **1999**, *156*, 373.
(5) Coquard, P.; Boistelle, R. *Int. J. Rock Mech. Min.* **1994**, *31*, 517.
(6) Russell, J. *Zement Kalk Gips* **1960**, *13*, 345.
(7) Hoxha, D.; Homand, F.; Auvray, C. *Eng. Geol.* **2006**, *86*, 1.
(8) Saadaoui, M.; Meille, S.; Reynaud, P.; Fantozzi, G. *J. Eur. Ceram. Soc.* **2005**, *25*, 3281.
(9) Chappuis, J. *Colloid Surf., A.* **1999**, *156*, 223.
(10) Arese, R.; Martin, D.; Rigaudon, M. *Process for reducing creep in a gypsum plaster-based element, gypsum plaster-based composition and method for making a gypsum plaster-based element with reduced creep.* U.S. Patent 2006/0048680, 2003
(11) Muller, R. E.; Henkels, P. L.; O' Kelly, B. M. *Gypsum board.* U.S. Patent 3 190 787, 1965.
(12) Yu, Q.; Sucech, S.; Groza, B.; Mlinac, R.; Jones, F.; Boehnert, F. *Process for reducing creep in a gypsum plaster-based element, gypsum plaster-based composition and method for making a gypsum plaster-based element with reduced creep.* U.S. Patent 6 632 550, 2003.
(13) Wilson, B. K.; Jones, K. W. *Production of shaped gypsum articles.* GB Patent 1 481 788, 1977.
(14) Badens, E.; Veesler, S.; Boistelle, R. *J. Cryst. Growth* **1999**, *198*, 704.
(15) Barwise, A. J.; Compton, R. G.; Unwin, P. R. *J. Chem. Soc., Faraday Trans.* **1990**, *86*, 137.
(16) Colombani, J. *Geochim. Cosmochim. Acta* **2008**, *72*, 5634.
(17) Jeschke, A. A.; Vosbeck, K.; Dreybrodt, W. *Geochim. Cosmochim. Acta* **2001**, *65*, 27.
(18) Compton, R. G.; Pritchard, K. L.; Unwin, P. R.; Grigg, G.; Silvester, P.; Lees, M.; House, W. A. *J. Chem. Soc., Faraday Trans. 1* **1989**, *85*, 4335.
(19) Compton, R. G.; Pritchard, K. L.; Unwin, P. R. *J. Chem. Soc., Chem. Commun.* **1989**, 249.

(20) Compton, R. G.; Unwin, P. R. *Philos. Trans. R. Soc. London, Ser. A* **1990**, *330*, 1.
(21) Compton, R. G.; Walker, C. T.; Unwin, P. R.; House, W. A. *J. Chem. Soc., Faraday Trans.* **1990**, *86*, 849.
(22) Unwin, P. R.; Compton, R. G. *J. Chem. Soc., Faraday Trans.* **1990**, *86*, 1517.
(23) Wilkins, S. J.; Compton, R. G.; Taylor, M. A.; Viles, H. A. *J. Colloid Interface Sci.* **2001**, *236*, 354.
(24) Thompson, M.; Wilkins, S. J.; Compton, R. G.; Viles, H. A. *J. Colloid Interface Sci.* **2003**, *259*, 338.
(25) Orton, R.; Unwin, P. R. *J. Chem. Soc., Faraday Trans.* **1993**, *89*, 3947.
(26) Brown, C. A.; Compton, R. G.; Narramore, C. A. *J. Colloid Interface Sci.* **1993**, *160*, 372.
(27) Hong, Q.; Suarez, M. F.; Coles, B. A.; Compton, R. G. *J. Phys. Chem. B* **1997**, *101*, 5557.
(28) Booth, J.; Sanders, G. H. W.; Compton, R. G.; Atherton, J. H.; Brennan, C. M. *J. Electroanal. Chem.* **1997**, *440*, 83.
(29) Peltonen, L.; Liljeroth, P.; Heikkila, T.; Kontturi, K.; Hirvonen, J. *Eur. J. Pharm. Sci.* **2003**, *19*, 395.
(30) Cooper, J. A.; Compton, R. G. *Electroanalysis* **1998**, *10*, 141.
(31) Snowden, M. E.; King, P. H.; Covington, J. A.; Macpherson, J. V.; Unwin, P. R. *Anal. Chem.* **2010**, *82*, 3124.
(32) Chung, D. D. L. *J. Mater. Sci.* **2003**, *38*, 2785.
(33) Deng, S. F.; Wang, C. F.; Zhou, Y.; Huang, F. R.; Du, L. *Mater. Sci. Eng., A* **2008**, *477*, 96.
(34) White, A. F.; Brantley, S. L. *Rev. Mineral* **1995**, *31*, 1.
(35) Luttge, A. *Am. Mineral.* **2005**, *90*, 1776.
(36) Unwin, P. R.; Macpherson, J. V. *Chem. Soc. Rev.* **1995**, *24*, 109.
(37) Vanysek, P. *CRC Handbook of Chemistry and Physics: Diffusion Coefficients and Ionic Conductivities*, 91st ed.; CRC Press Taylor & Francis: Boca Raton, FL, 2010−2011.
(38) Mbogoro, M. M.; Snowden, M. E.; Edwards, M. A.; Peruffo, M.; Unwin, P. R. *J. Phys. Chem. C* **2011**, *115*, 10147.
(39) Singh, N. B.; Middendorf, B. *Prog. Cryst. Growth Charact. Mater.* **2007**, *53*, 57.
(40) Jaffel, H.; Korb, J. P.; Ndobo-Epoy, J. P.; Morin, V.; Guicquero, J. P. *J. Phys. Chem. B* **2006**, *110*, 7385.
(41) Freyer, D.; Voigt, W. *Monatsh. Chem.* **2003**, *134*, 693.
(42) Hughes, T.; Methven, C.; Jones, T.; Pelham, S.; Fletcher, P.; Hall, C. *Adv. Cem. Based Mater.* **1995**, *2*, 91.
(43) Han, H. J.; Kim, D. P. *J. Sol−Gel Sci. Technol.* **2003**, *26*, 223.
(44) Socrates, G. *Infrared Characteristic Group Frequencies*; John Wiley & Sons: Chichester, U.K., 1980.
(45) Brow, R. K. In *15th University Conference on Glass Science*; Elsevier Science Bv: Rolla, MO, 1999; p 1.
(46) Metwalli, E.; Brow, R. K. *J. Non-Cryst. Solids* **2001**, *289*, 113.
(47) de Jongh, P.; van Tilborg, P.; Wondergem, H. *J. Sol−Gel Sci. Technol.* **2004**, *31*, 241.
(48) Tricot, G.; Coillot, D.; Creton, E.; Montagne, L. *J. Eur. Ceram. Soc.* **2008**, *28*, 1135.
(49) Brandt, F.; Bosbach, D. *J. Cryst. Growth* **2001**, *233*, 837.
(50) Bruckenstein, S.; Sharkey, J. W.; Yip, J. Y. *Anal. Chem.* **1985**, *57*, 368.
(51) Unwin, P. R.; Compton, R. G. *J. Electroanal. Chem.* **1988**, *245*, 287.
(52) Finot, E.; Lesniewska, E.; Mutin, J. C.; Goudonnet, J. P. *Langmuir* **2000**, *16*, 4237.
(53) Kato, Y.; Matsui, M; Umeya, K *Gypsum Lime* **1980**, *166*, 83.
(54) Reynaud, P.; Saadaoui, M.; Meille, S.; Fantozzi, G. In *ICIFMS-14*; Elsevier Science Sa: Kyoto, Japan, 2005, p 500.
(55) Hill, J. R.; Plank, J. *J. Comput. Chem.* **2004**, *25*, 1438.
(56) van der Voort, E.; Hartman, P. *J. Cryst. Growth* **1991**, *112*, 445.